Whistler mode wave growth and propagation in the prenoon magnetosphere

Article

Published Version

Watt, C. E. J., Rankin, R. and Degeling, A. W. (2012) Whistler mode wave growth and propagation in the prenoon magnetosphere. Journal of Geophysical Research, 117. A06205. ISSN 0148-0227 doi: 10.1029/2012JA017765 Available at https://centaur.reading.ac.uk/32797/

Published version at: http://dx.doi.org/10.1029/2012JA017765
To link to this article DOI: http://dx.doi.org/10.1029/2012JA017765

Publisher: American Geophysical Union

Whistler mode wave growth and propagation in the prenoon magnetosphere

C. E. J. Watt,[1] R. Rankin,[1] and A. W. Degeling[1]

Received 26 March 2012; accepted 23 April 2012; published 5 June 2012.

[1] Pitch angle scattering of electrons can limit the stably trapped particle flux in the magnetosphere and precipitate energetic electrons into the ionosphere. Whistler mode waves generated by a temperature anisotropy can mediate this pitch angle scattering over a wide range of radial distances and latitudes, but in order to correctly predict the phase space diffusion, it is important to characterize the whistler mode wave distributions that result from the instability. We use previously published observations of number density, pitch angle anisotropy, and phase space density to model the plasma in the quiet prenoon magnetosphere (defined as periods when $AE < 100$ nT). We investigate the global propagation and growth of whistler mode waves by studying millions of growing raypaths and demonstrate that the wave distribution at any one location is a superposition of many waves at different points along their trajectories and with different histories. We show that for observed electron plasma properties, very few raypaths undergo magnetospheric reflection; most rays grow and decay within 30 degrees of the magnetic equator. The frequency range of the wave distribution at large L can be adequately described by the solutions of the local dispersion relation, but the range of wave normal angle is different. The wave distribution is asymmetric with respect to the wave normal angle. The numerical results suggest that it is important to determine the variation of magnetospheric parameters as a function of latitude, as well as local time and L-shell.

Citation: Watt, C. E. J., R. Rankin, and A. W. Degeling (2012), Whistler mode wave growth and propagation in the prenoon magnetosphere, *J. Geophys. Res.*, *117*, A06205, doi:10.1029/2012JA017765.

1. Introduction

[2] The pitch angle scattering of particles by electromagnetic waves is an important loss mechanism in the magnetosphere [e.g., *Schulz and Lanzerotti*, 1974]. Trapped particles executing bounce motion between hemispheres can be lost to the atmosphere if, at some point along their trajectory, wave-particle interactions cause their pitch angle to be decreased such that the particle falls into the loss cone. Candidate wave modes for this process include electromagnetic ion cyclotron (EMIC) waves, electrostatic electron cyclotron harmonic (ECH) waves, and whistler mode waves. EMIC waves have left-hand polarization, and have the lowest frequencies in this group, clustering around the ion gyrofrequencies of each ion species present in the magnetosphere. They resonate with high-energy electrons (> 500 keV) [*Horne and Thorne*, 1998; *Summers and Thorne*, 2003; *Jordanova et al.*, 2008; *Miyoshi et al.*, 2008]. In contrast, ECH waves have much higher frequencies, between the harmonics of the electron cyclotron frequency Ω_e, and resonate with particles in the 0.1–10 keV range [e.g., *Horne and Thorne*, 2000]. Whistler mode waves have frequencies less than Ω_e, exhibit right-hand polarization, and resonate with electrons which have a broad range of energies, from a few hundred up to several MeV. This broad range of resonant energies suggests that whistler mode waves are important for pitch angle scattering throughout the terrestrial magnetosphere [*Kennel and Petschek*, 1966; *Tkalcevic et al.*, 1984; *Inan*, 1987; *Villalon and Burke*, 1995; *Faith et al.*, 1997a, 1997b; *Liemohn et al.*, 1997; *Abel and Thorne*, 1998; *Horne and Thorne*, 1998; *Lorentzen et al.*, 2001; *Kirkwood and Osepian*, 2001; *Chen and Schulz*, 2001; *Horne and Thorne*, 2003; *Horne et al.*, 2003; *Summers et al.*, 2004; *Thorne et al.*, 2005; *Shprits et al.*, 2006; *Summers et al.*, 2007a, 2007b; *Kuo et al.*, 2007; *Summers et al.*, 2008; *Ni et al.*, 2008; *Tadokoro et al.*, 2009; *Meredith et al.*, 2009; *Lam et al.*, 2010; *Miyoshi et al.*, 2010; *Su et al.*, 2010; *Thorne et al.*, 2010] and the magnetospheres of other magnetized planets [*Xiao et al.*, 2003; *Bhattacharya et al.*, 2005; *Tripathi and Singhal*, 2008; *Radioti et al.*, 2009; *Summers et al.*, 2009].

[3] The precipitation of particles due to whistler mode wave mediated pitch angle scattering is a possible candidate for the self limitation of stably trapped particle fluxes in planetary magnetospheres [*Kennel and Petschek*, 1966; *Summers et al.*, 2009]. The modulation of 30 keV–300 keV particle precipitation by ultra low frequency (ULF) waves [*Ziauddin*, 1960; *Anger et al.*, 1963; *Brown*, 1964; *Parthasarathy and Hessler*,

[1]Department of Physics, University of Alberta, Edmonton, Alberta, Canada.

Corresponding author: C. E. J. Watt, Department of Physics, University of Alberta, Edmonton, AB T6G 2G7, Canada. (watt@ualberta.ca)

0148-0227/12/2012JA017765

1964; *Hargreaves*, 1969; *Yuan and Jacka*, 1969; *Hunsucker et al.*, 1972; *Berkey*, 1974; *Brown*, 1975; *Heacock and Hunsucker*, 1977; *Olson et al.*, 1980; *Paquette et al.*, 1994; *Posch et al.*, 1999; *Spanswick et al.*, 2005; *Rae et al.*, 2007; *Roldugin and Roldugin*, 2008] is thought to occur once a steady precipitation rate has been established. *Coroniti and Kennel* [1970] suggest that this steady precipitation may be accomplished by whistler mode waves. Under the action of slow ULF wave variations, the whistler mode growth rates are gradually modified, leading to variations in the pitch angle diffusion and hence the precipitation. The pitch angle scattering which maintains trapped particle fluxes in the magnetosphere, or forms some kind of steady background precipitation, is likely to be due to some marginal instability which exists over an extended region in the magnetosphere. This process is thought to create a delicate balance between a source of electrons, a weakly driven whistler mode wave instability and the resulting electron precipitation, and is probably different from the stronger, nonlinear instabilities which are responsible for chorus generation [e.g., *Santolík et al.*, 2003; *Katoh and Omura*, 2007; *Omura et al.*, 2008; *Hikishima et al.*, 2009a; *Katoh and Omura*, 2011].

[4] Pitch angle diffusion can be modeled using quasi-linear diffusion coefficients [*Lyons*, 1974a, 1974b; *Inan et al.*, 1992; *Villalon and Burke*, 1995; *Albert*, 1999, 2005; *Glauert and Horne*, 2005; *Summers et al.*, 2008; *Ni et al.*, 2008; *Su et al.*, 2010]; however, these diffusion coefficients require wave information as a function of frequency and wave normal angle. Comprehensive models of the diffusion process therefore require realistic models of the wave spectra. It is possible to obtain whistler mode wave spectra from in situ measurements as functions of wave normal angle and propagation angle [*Hayakawa et al.*, 1986; *Hospodarsky et al.*, 2001; *Santolík et al.*, 2009; *LeContel et al.*, 2009; *Agapitov et al.*, 2010]. Most often, these measurements are of chorus elements, which may have a different generation mechanism than the weak instabilities considered here. Additionally, in situ measurements are often single point measurements, or tightly clustered measurements, and cannot indicate how wave spectra vary over large distances along or across field lines. It is unlikely that a spacecraft will remain in the same location long enough to monitor how wave spectra change due to, say, long-period ULF wave variations. Hence accurate models of whistler mode wave distributions are required which can simultaneously describe the waves in different regions of the magnetosphere and that can respond to slow changes in field and plasma properties. Ray tracing is an obvious candidate to build up a picture of whistler mode waves and has successfully been used to describe whistler mode wave propagation throughout the magnetosphere and plasmasphere [e.g., *Inan and Bell*, 1977; *Thorne et al.*, 1979; *Church and Thorne*, 1983; *Huang and Goertz*, 1983; *Huang et al.*, 1983; *Chum et al.*, 2003; *Chum and Santolík*, 2005; *Bortnik et al.*, 2006, 2007a, 2007b, 2008; *Li et al.*, 2008, 2009; *Bortnik et al.*, 2011a, 2011b]. Previous ray tracing studies predict that the angle between whistler mode wave vectors and the magnetic field can vary significantly as the wave travels through the magnetosphere, and that the propagation of the waves is close to, but not directly along, the magnetic field. It is possible, therefore, that the wave spectra at any one location is a superposition of multiple waves from multiple source locations, all traveling along different paths and at different stages in their evolution. Realistic models of whistler mode wave spectra therefore require a nonlocal approach which includes waves which are driven unstable at multiple locations in the magnetosphere and which follow multiple paths.

[5] This article describes the growth and propagation of whistler mode waves through the magnetosphere given conditions for whistler mode growth near the magnetic equator. We focus on periods of low activity in the magnetosphere, in order to benchmark future studies of whistler mode wave growth during more active times. Observations reported by *Li et al.* [2010] are used to constrain the number density, temperature and anisotropy of energetic electrons in the region between L = 5 and L = 10 between 6 and 12MLT where whistler mode waves are often observed. We use geometric ray tracing to follow the paths of millions of unstable whistler mode waves. A linear kinetic dispersion relation is used to follow the path-integrated gain of the waves along their path. Key information (wave gain, frequency, local wave normal direction, local group velocity direction, and wave origin) is collected in bins arrayed in L-shell and latitude. We will use these results to argue that the latitudinal profile of energetic electron properties is key to understanding whistler mode growth in the magnetosphere.

[6] In the next section, we describe the plasma model, as derived from field and plasma observations from the THEMIS spacecraft [*Li et al.*, 2010]. Section 3 presents details of the wave propagation model, and the method for calculating the path-integrated gain. Ray tracing results are presented in section 4. We discuss the results from the model in section 5, before presenting our conclusions in section 6.

2. Plasma Model During Quiet Magnetospheric Periods

[7] *Li et al.* [2010] present a survey of inner magnetospheric data from the THEMIS spacecraft. They sort their observations by the AE index as a proxy for magnetospheric activity. We focus on quiet times (AE < 100 nT), and on observations taken outside the plasmasphere to benchmark future analyses.

[8] We construct an idealized dipole model of the magnetospheric magnetic field between L = 5 and L = 10 and use plasma observations between 6 and 12 MLT to constrain our plasma model, since this is where most of the whistler mode wave activity is observed [*Li et al.*, 2010, Figure 1]. Note that previous studies have shown that whistler mode waves can travel great distances through the magnetosphere, and can undergo magnetospheric reflection [e.g., *Kimura*, 1966], and so it is important that our number density model is realistic over a large volume of the magnetosphere. We use a modified diffusive equilibrium model for the electron number density N_e [*Inan and Bell*, 1977], similar to models used by *Bortnik et al.* [2006, 2007a, 2007b, 2011a], and details are given in Appendix A. Whistler mode growth depends on the temperature anisotropy A, the temperature of the energetic electron component T_e, and on the ratio of the plasma frequency to the gyrofrequency ω_{pe}/Ω_e [*Watt et al.*, 2011]. *Li et al.* [2010] show that ω_{pe}/Ω_e varies slowly between around 3 and 7 for 6–12 MLT. Our choice of parameters for the number density model gives an equatorial density variation as shown in Figure 1a, and the corresponding variation of ω_{pe}/Ω_e is shown in Figure 1b, which closely reproduces

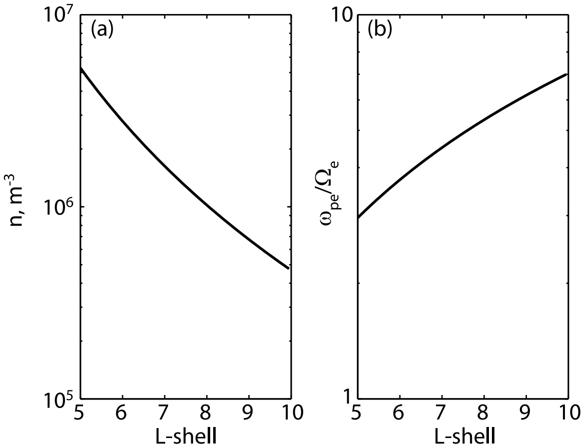

Figure 1. (a) Modeled equatorial number density N_e and (b) ω_{pe}/Ω_e as a function of L-shell (cf. data presented between 6 and 12 MLT in *Li et al.* [2010, Figures 1a and 1b]).

properties obtained from the *Li et al.* [2010] survey of THEMIS measurements.

[9] The distribution of warm/hot electrons which provide the plasma instability are more difficult to model. Typically, energy distributions are modeled by a sum of Maxwellian components of different density, temperature and anisotropy [see, e.g., *Li et al.*, 2009]. Clearly, any number of components may be chosen to obtain increasingly accurate fits. *Li et al.* [2010, Figure 4] show the mean equatorial anisotropy (A), and omnidirectional phase space density (PSD) as a function of energy, local time and L-shell for periods of low magnetospheric activity. For energies between 0.5 keV and 10 keV, the anisotropy increases with L, peaking at $A \sim 0.6$ around $L = 8$, before decreasing slightly toward $L = 10$. At higher energies (10–100 keV), the anisotropy increases gradually with L for $L < 8$, before increasing sharply toward $L = 10$, where $A \sim 0.7$. Using these statistical equatorial anisotropy observations as a guide, we have constructed a model of warm electrons with two components: population 1 has a temperature of $T_{\parallel} = 1.4$ keV, and population 2 has a temperature of $T_{\parallel} = 10$ keV. The variation of the equatorial anisotropies of the two populations are shown in Figure 2a, and are given by $A_{\mathrm{eq},1} = 0.004\, w^3 + 0.2\, w$ and $A_{\mathrm{eq},2} = 0.0061\, w^3$, where $w = (r_{eq}/R_E) - 5$, and r_{eq} is the radial distance at the equator. Given the modeled variation in anisotropy of the two components, the equatorial number density of each component was modeled with the help of the equatorial omnidirectional PSD from *Li et al.* [2010]. Maxwellian distributions were constructed with the temperature properties given above, and the omnidirectional PSD calculated as a function of L-shell for different number density profiles until rough agreement was obtained with the observations. With our crude two-component model, we have aimed to reproduce general trends and obtain agreement with the statistical survey data to within a factor of two. Note that Maxwellian distribution functions cannot reproduce the large changes in the value of PSD between 10–30 keV and 30–100 keV as shown in *Li et al.* [2010, Figure 4], which indicates a drop of nearly two orders of magnitude between the two energy ranges at low L. We suggest that the large difference in PSD between these two energy ranges may be due to calibration differences between the THEMIS ESA instrument (used for the 10–30 keV observations) and the THEMIS SST instrument (used for the 30–100 keV observations). If we focus instead on the trends in the observations, then *Li et al.* [2010] show that the prenoon omnidirectional PSD is essentially flat as a function of L for energies between 0.5 keV and 10 keV, and decreases with L for the highest energies (30–100 keV). The resulting modeled number densities are $n_{\mathrm{eq},1} = 10^5 + 3.0 \times 10^5\, w$ and $n_{\mathrm{eq},2} = 5.0 \times 10^4 - 8.0 \times 10^3\, w$, and are shown in Figure 2b. Note that the fraction of the electron energy density composed of warm electrons increases with L-shell (Figure 2c). The modeled equatorial omnidirectional PSD is shown in Figure 3 for comparison with the observations presented in *Li et al.* [2010].

[10] The modeled equatorial plasma variables in Figure 2 are extended to higher latitudes under the assumption that the idealized behavior of bouncing electrons in the dipole magnetic field can accurately describe the variation of number density and temperature with latitude λ [see, e.g., *Xiao and Feng*, 2006]. Under this assumption, the parallel temperature does not vary with λ, whereas the number density and perpendicular temperatures vary as

$$[n(\lambda)]_{1,2} = [n_{\mathrm{eq}}]_{1,2} \left[\frac{v^2_{\mathrm{eq},\perp}}{v^2_{\perp}(\lambda)}\right]_{1,2} \tag{1}$$

and

$$[v^2_{\perp}(\lambda)]_{1,2} = [v^2_{\mathrm{eq},\perp}]_{1,2} \left[\frac{1-\Delta_e}{1-\Delta_e B_{\mathrm{eq}}/B(\lambda)}\right], \tag{2}$$

where $\Delta_e = 1 - [v^2_{\mathrm{eq},\parallel}/v^2_{\mathrm{eq},\perp}]_{1,2}$, $B(\lambda)$ is the local magnetic field strength, and B_{eq} is the equatorial magnetic field strength along the same field line. The temperature anisotropy $A = v^2_{\perp}/v^2_{\parallel} - 1$, where $v_{\perp,\parallel} = (2k_b T_{\perp,\parallel}/m_e)^{1/2}$ are the perpendicular and parallel thermal speeds, respectively. The

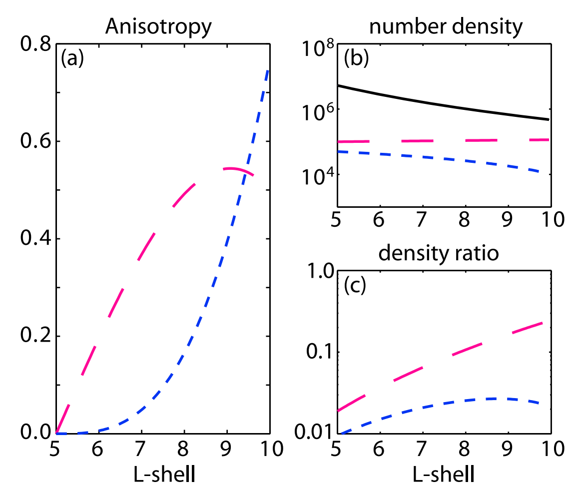

Figure 2. (a) Modeled equatorial electron anisotropy for population 1 (red dashed line, $T_{\parallel,1} = 1.4$ keV) and population 2 (blue dashed line, $T_{\parallel,2} = 10$ keV). (b) Total modeled number density (black solid line) with number densities of population 1 (red dashed line) and population 2 (blue dashed line) at the equator. (c) Modeled density ratios $n_{\mathrm{eq},1}/N_E$ (red dashed line) and $n_{\mathrm{eq},2}/N_e$ (blue dashed line).

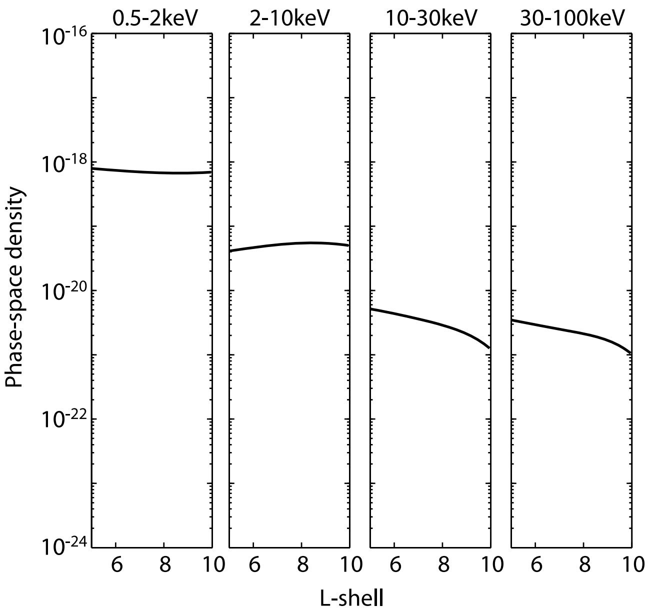

Figure 3. Variation of modeled equatorial omnidirectional phase space density (PSD) as a function of L for 0.5–2.0 keV, 2–10 keV, 10–30 keV, and 30–100 keV (cf. data presented between 6 and 12 MLT in *Li et al.* [2010, Figure 4]).

latitudinal variation in anisotropy of each population is shown in Figure 4.

3. Whistler Mode Wave Propagation Model

3.1. Ray-Tracing Model

[11] It has been repeatedly shown that structured whistler mode emissions in the magnetosphere (i.e., whistler mode chorus) are most likely due to the nonlinear interaction between trapped electrons and whistler mode emissions in an inhomogeneous magnetic field [*Katoh and Omura*, 2007; *Trakhtengerts and Rycroft*, 2008; *Omura et al.*, 2008, 2009; *Hikishima et al.*, 2009a, 2009b]. Fully self-consistent non-periodic kinetic models show that the generation of parallel-propagating whistler mode waves has both a linear and a nonlinear phase [*Omura et al.*, 2008; *Hikishima et al.*, 2009a]. Previous studies have made it clear, however, that a fully nonlinear three-dimensional simulation of the wave-particle interactions over large regions of the magnetosphere is impossible given current computing resources [*Nunn et al.*, 2009] so fully self-consistent models must be constrained to study waves with parallel wave vectors and parallel group velocities only.

[12] In order to study both the parallel and oblique propagation of whistler mode waves over an extended region of the magnetosphere, we simplify the problem by using the cold plasma ray-tracing equations [e.g., *Kimura*, 1985] to predict the propagation of the waves. The path-integrated gain of these waves is estimated using the warm plasma dispersion relation to calculate the linear growth rates along these raypaths. This approach has been successfully used in other studies [*Bortnik et al.*, 2006, 2007a, 2007b, 2008; *Li et al.*, 2008, 2009; *Breneman et al.*, 2009; *Bortnik et al.*, 2011a] to study the behavior of whistler mode waves in the inhomogeneous magnetosphere. We assume an idealized axisymmetric dipolar magnetic field and solve the two-dimensional ray-tracing equations [e.g., *Walter*, 1969]

$$\frac{dr}{dt} = \frac{c}{\mu}(\cos\delta - \tan\alpha \sin\delta), \tag{3}$$

$$\frac{d\theta}{dt} = \frac{c}{r\mu}(\sin\delta + \tan\alpha \cos\delta), \tag{4}$$

$$\frac{d\delta}{dt} = -\frac{c}{\mu^2}\left(\frac{\partial\mu}{\partial r}\sin\delta - \frac{1}{r}\frac{\partial\mu}{\partial\theta}\cos\delta\right) - \frac{c}{r\mu}\sin\delta, \tag{5}$$

where c is the speed of light in a vacuum, r is the radial coordinate and θ is the colatitude coordinate of the raypath, μ is the phase refractive index, t is the phase time of the principal wave, α is the angle between the wave normal and the group velocity vector and δ is the angle between the radial vector and the wave normal. All angles are positive in the clockwise direction. μ is calculated from the cold plasma approximation [see, e.g., *Stix*, 1992]. We have validated this approximation by comparing the real part of solutions from the cold plasma dispersion relation and the full warm plasma dispersion relation [e.g., *Horne and Thorne*, 1998]. Figure 5 (top) shows the real frequency solutions for parallel wave normal angle at the equator for increasing values of L. Circles show the solutions for a cold plasma, and the line indicates the solutions from the full warm plasma dispersion relation. In this instance, the cold plasma approximation to μ is sufficient.

[13] Equations (3)–(5) are solved using a step-adaptive Runge-Kutta method [e.g., *Press et al.*, 2007]. Note that for simplicity in the results to follow, we will use the radius r and the latitude λ to describe position in the model, even though individual ray tracing calculations use the colatitude. In this paper, we limit the analysis to a two-dimensional meridianal plane of our idealized dipolar magnetosphere. Future work will extend the ray tracing in the azimuthal direction and introduce more realistic magnetospheric topology. However, for the magnetospheric regime modeled in this paper, azimuthal gradients in the prenoon sector are observed to be small [see *Li et al.*, 2010, Figure 1].

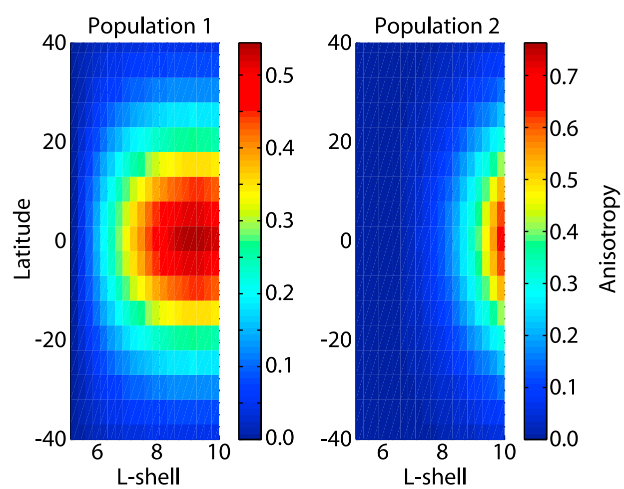

Figure 4. Variation of anisotropy for each modeled population as a function of L and latitude.

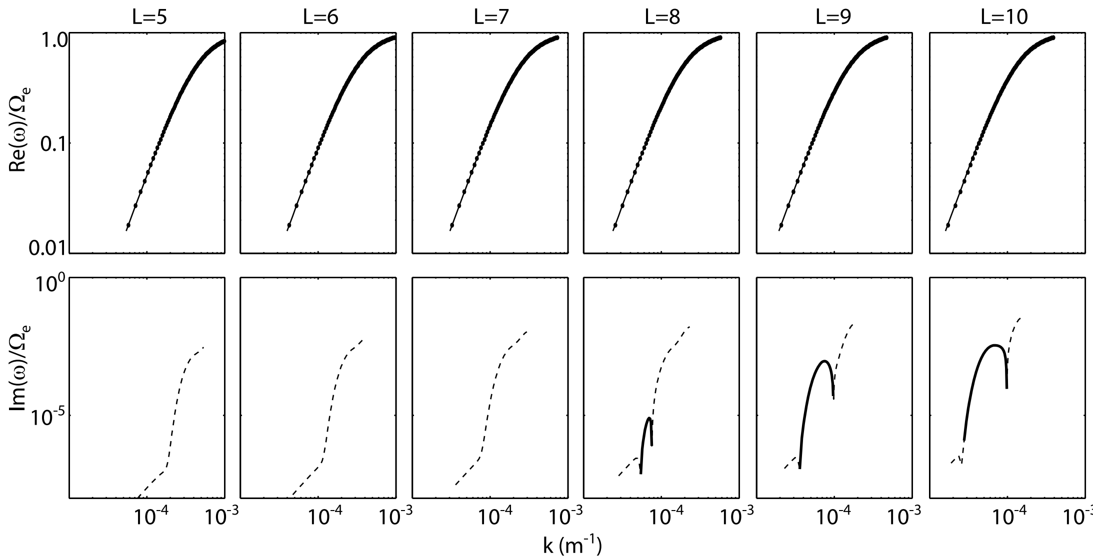

Figure 5. Local solutions at the equator to the full linear warm dispersion relation as a function of L. (top) The real part of the frequency (solid line gives full solution, and dots give solution to the cold plasma dispersion relation) and (bottom) the imaginary part (solid line indicates growing waves and dashed line indicates damped waves). All solutions are normalized to the local electron gyrofrequency.

[14] We have used previous published results to benchmark the ray tracing algorithm [*Church and Thorne*, 1983; *Huang and Goertz*, 1983; *Huang et al.*, 1983; *Li et al.*, 2008, 2009], and where sufficient information about the number density model is provided, we have been able to satisfactorily reproduce the raypaths shown.

3.2. Path-Integrated Gain of Whistler Mode Waves

[15] The warm plasma component model is used to calculate the growth rates for the wave at every calculated step along the raypath. We solve the full linear warm plasma dispersion relation [e.g., *Horne and Thorne*, 1998] for complex wave number, given the wave frequency and the local magnetic field strength, cold plasma number density, and warm plasma parameters according to the models detailed above. Figure 5 (bottom) shows the imaginary part of the solutions to the local linear dispersion relation for parallel wave normal vector at the equator at different L-shells in our model. The solid line indicates growing (positive) solutions and the dashed line indicates damped (negative) solutions. The local analysis suggests that waves will only grow for $L \geq 8$; at lower L-shells they are heavily damped since the temperature anisotropy is small.

[16] Observations point to the equator as a source for whistler mode waves [*Muto and Hayakawa*, 1987; *Muto et al.*, 1987; *Nagano et al.*, 1996; *LeDocq et al.*, 1998; *Hospodarsky et al.*, 2001], but the measurement of electromagnetic waves at any particular point in situ is likely to represent a superposition of waves with different amplitudes traveling in different directions from different source locations. Under these circumstances, the largest contributions to the wave fields at the spacecraft may indicate wave propagation in a single direction, but in fact the waves present are from multiple sources [e.g., *Santolík et al.*, 2001]. Where other ray tracing investigations have studied the propagation of whistler mode waves injected at the magnetospheric equator [*Bortnik et al.*, 2007b], or back traced waves only as far as the equator [*Parrot et al.*, 2003, 2004; *Hayosh et al.*, 2010], we model the wave growth assuming that unstable plasma conditions could also exist away from the equator (see Figure 4).

[17] Wave gain G (in decibels) is calculated from the integral of the convective growth along each raypath [e.g., *Horne and Thorne*, 1997]

$$G(s_1) = 8.6859 \int_{s_0}^{s_1} -(k_i \cos\alpha) ds, \tag{6}$$

where s is the distance along a raypath from the start s_0 to the point s_1, k_i is size of the complex part of the wave number at the point s, and α is the angle between the group velocity v_g and the wave vector [cf. *Bekefi*, 1966, equation 1.129]. Ray tracing would be automatically stopped in our analysis if $\omega_i = -k_i v_g$ became larger than 0.1 ω_r, but for our model of warm plasma (see previous section), we find that $\omega_i \ll \omega_r$ at all locations in the numerical domain.

[18] Figure 6a shows the growing paths obtained from two source locations at $r_0 = 8.5\ R_E$ and $r_0 = 9.5\ R_E$, $\lambda = -5°$. By varying the wave normal angle ψ (the angle between the wave vector and the local magnetic field direction), the range of growing modes at each location can be investigated. If waves have positive growth rates at the source locations, then they are followed until their path-integrated gain becomes negative. If we assume these waves grow out of local thermal noise, then this would be the point at which the waves would no longer contribute any physical effect. The color indicates G as the wave propagates through the inhomogeneous plasma. The largest gain for these two groups of raypaths is 40 dB. The waves propagate in directions close to the magnetic field direction (indicated with dashed lines). Figures 6b and 6e show the evolution of the wave normal angle ψ for these two families of raypaths. All angles are measured clockwise relative to the local magnetic field direction. The wave normal slowly changes as the wave

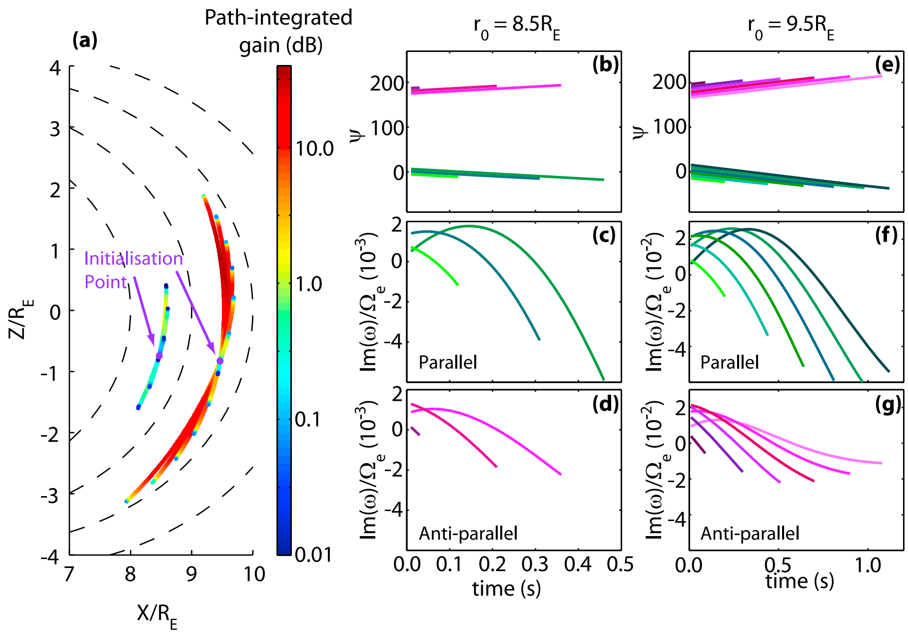

Figure 6. (a) Trajectories of growing raypaths started at $r_0 = 8.5\ R_E$ and $r_0 = 9.5\ R_E$ with $\lambda = -5°$. Colors indicate the path-integrated gain. Coordinate Z is aligned with the magnetic north pole and coordinate X is aligned along the magnetic equator. (b and e) Evolution of the wave normal angle along each raypath. (c and f) Growth rates of the parallel-propagating rays. (d and g) Growth rates of the antiparallel-propagating rays.

propagates, turning as predicted by many previous studies [e.g., *Thorne et al.*, 1979; *Bortnik et al.*, 2007a, 2007b; *Li et al.*, 2009]. Figures 6c and 6f show the growth rates for the parallel propagating rays and Figures 6d and 6g show the growth rates for the antiparallel propagating rays. As expected, the largest growth rates occur as the waves propagate through the equator, where the temperature anisotropies are greatest.

4. Two-Dimensional Distribution of Wave Gain in the Magnetosphere

[19] We build up a picture of whistler mode wave propagation and growth in the magnetosphere by initiating millions of raypaths in the magnetosphere. Ray starting points are randomly chosen inside a region with $5 < L < 10$ and $-30° < \lambda < +30°$. Results do not change if we extend the study region in latitude, and we cover L-shells for which we have observational constraints on the warm plasma model. The real frequencies ω_r are also randomly chosen such that $0.05\Omega_e < \omega_r < 0.55\Omega_e$, where $\Omega_e = |q_e|B_0/m_e$ is the absolute value of the local electron gyrofrequency. Given our model of unstable electron distribution functions (see section 2), this range of initial frequencies more than adequately covers the range of growing waves possible. From each of the randomly chosen initial positions, 36 raypaths are initiated, each of which is given a different initial angle ψ relative to the local magnetic field at 10° intervals between 0° and 360°. Only raypaths which result in growing waves are followed, and their position, direction of propagation, direction of wave vector relative to the local field and path-integrated wave gain are tracked and binned on a grid in L and λ with cells of $0.25L$ and 5°. Information from each raypath is only binned once in any particular cell and raypaths are no longer followed after G becomes negative. The results are not changed significantly when the cell size of the numerical domain is reduced. It is assumed that the wave distribution is time stationary, and so waves can be generated at any time. The wave distribution at any location therefore has contributions from waves at many different points along their trajectories. The group time between the initial and end points of the raypaths used in this study is typically found to be less than 2 s. More than 10^7 initialized raypaths resulted in over one million separate binning events, with at most ~40,000 information points in a single cell.

[20] As an overview of the results, Figure 7 shows the maximum value of G in each L-latitude cell. As expected from the local analysis (Figure 5), growing wave paths are

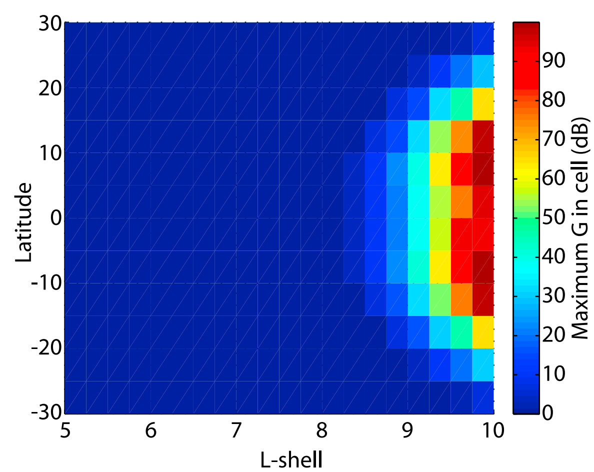

Figure 7. Maximum path-integrated gain in each L-latitude cell after $>10^7$ raypaths have been initiated.

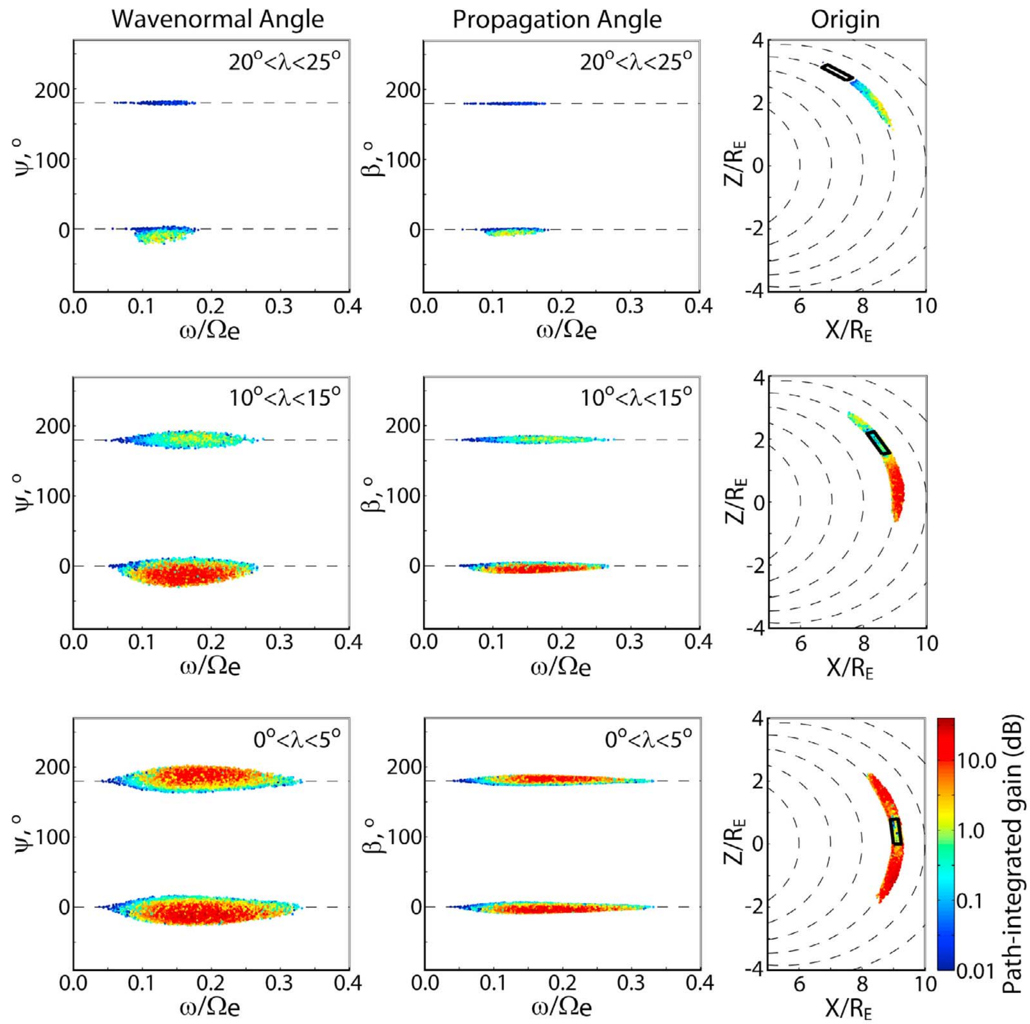

Figure 8. Wave gain as a function of (left) normalized frequency and wave normal angle, (middle) normalized frequency and propagation angle, and (right) initialization location, for three different cells with $9.0 < L < 9.25$: (top) $20° < \lambda < 25°$, (middle) $10° < \lambda < 15°$ and (bottom) $0° < \lambda < 5°$. The color scale for G is the same in each panel. The black rectangles in the "Origin" panels indicate the cell where the gains are recorded.

confined to $L > 8$. *Chen et al.* [2009] suggest that at least 40 dB of wave gain is required to allow waves to grow to observable levels from the background noise. The model predicts that this would only occur for $L > 9$ and for $-20° < \lambda < 20°$. Interestingly, G is not always largest near the equator, but often maximizes in the $5° < |\lambda| < 10°$ cells. The reason for this can be deduced from Figure 6: maximum growth will occur near the equator, but maximum G will occur at the point at which the growth rate changes from positive to negative. These points are separated in latitude.

[21] The distribution of G in frequency can provide information regarding the wave distribution in any particular cell. Figure 8 shows G for cells with $9.0 < L < 9.25$ at three different latitudes (results are symmetric with respect to the equator). G is displayed as a function of normalized frequency and wave normal angle in the left column, normalized frequency and propagation angle in the central column, and initialization location in the right column. The raypaths in each bin form a true superposition of waves; we found many raypaths in the same cell with different G and different histories, but similar ω_r and ψ. Results shown in these plots have been selected from narrow bins in ω_r and ψ in order to isolate the rays with the largest gain.

[22] Near the equator, the wave distributions with parallel and antiparallel ψ are essentially symmetric. This is also true for the wave distributions as a function of the propagation angle, β. At $10° < \lambda < 15°$, the waves with largest values of G have wave vectors that cluster around the parallel direction, and propagate away from the equator. Few raypaths reach the highest-latitude cells in the numerical domain before their gain becomes negative, and we found no reflecting raypaths in the analysis. Figure 8 (right) shows that the wave distribution at any particular latitude depends upon the plasma conditions at a different latitude. The largest amplitude waves at the equator originate at higher latitude, whereas the largest amplitude waves at the $10° < \lambda < 15°$ cell originate near the equator.

[23] The largest values of G do not occur for rays with $\psi = 0$, as predicted by the local solutions of the linear dispersion relation. Figure 9a reproduces the bottom left panel

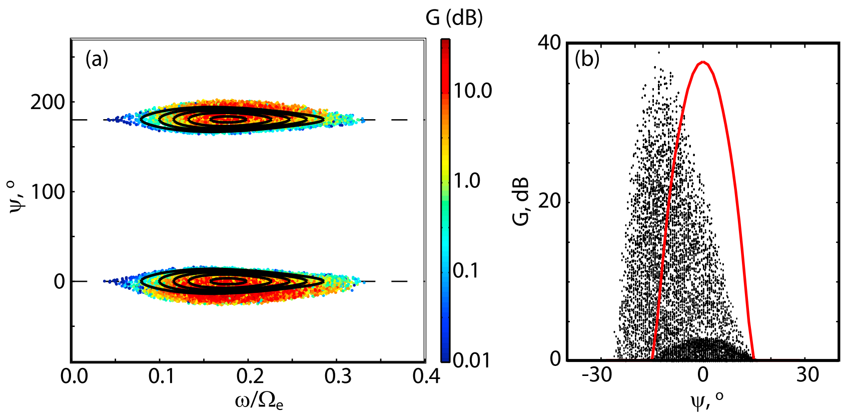

Figure 9. (a) Wave gain as a function of normalized frequency and wave normal angle for $9.0 < L < 9.25$ and $0° < \lambda < 5°$. Black contours represent growing solutions of the local plasma dispersion relation in the middle of this cell. (b) Scatterplot of path-integrated gain as a function of wave normal angle for quasi-parallel ψ. The red line indicates the functional form of the growing solutions of the local dispersion relation.

of Figure 8, and shows contours of solutions to the local warm plasma dispersion relation. Only growing solutions are shown, and the local solutions peak at $\psi = 0°$ and $\psi = 180°$. The frequency range of raypaths with large G (note that we use a logarithmic scale in Figure 9a) are approximated very well by the solutions of the local dispersion relation, but the range of wave normal angles is very different. Figure 9b presents a scatterplot of all the wave gains as a function of ψ for the quasi-parallel wave vectors (Figure 9a is essentially symmetric around $\psi = 90°$). The red line shows the solutions to the local dispersion relation for $\omega/\Omega_e = 0.17$, where the growth rates maximize. The values of G shown in Figure 9b appear to form two groups: in the middle of the plot there is a group of raypaths with $G < 4$ dB which has similar characteristics to the solutions of the local dispersion relation, peaking at $\psi = 0°$ and extending to $\psi \pm 15°$. The second group of raypaths has much higher values of G, up to $G = 40$ dB, and is skewed toward negative ψ.

5. Discussion

[24] *Li et al.* [2010] use their survey of electromagnetic emission from THEMIS to show that during periods of low activity, low-amplitude whistler mode wave activity is limited to $L > 7$ and peaks around $L = 9$. Using a model of plasma density, temperature and anisotropy based upon the same THEMIS survey, and by tracing millions of linear raypaths through an idealized magnetosphere, we find that whistler mode wave activity is limited to $L > 8$ and peaks at $L = 10$. Future work will investigate how sensitive our results are to the plasma model used. The equatorial values of the number density, temperature anisotropy and phase space density were constrained by a THEMIS survey [*Li et al.*, 2010]. However, the latitudinal variation of these parameters was modeled with fewer constraints. For example, the model described in this paper imposed a dipole magnetic field configuration at all L-shells. *Tsurutani and Smith* [1977] suggest that the generation of whistler mode waves on the dayside could occur in two minimum B pockets, created due to the compression of the dayside magnetosphere by the solar wind. Whistler mode waves would then be generated preferentially at latitudes away from the equator. The latitudinal variation of anisotropy and warm electron number density used in this study was based upon the behavior of bouncing electrons in the dipolar magnetic field assuming they are unaffected by any other forces. Clearly, the behavior of electrons will be affected by the presence of the very waves that this model examines. Whistler mode wave growth acts to limit the anisotropy that forms the free energy source through pitch-angle diffusion [*Gary and Wang*, 1996]. However, the latitudinal variation of the pitch angle diffusion that results from wave-particle interactions will be governed by the amplitude of the waves at each latitude. Figure 7, which shows the maximum gain in each cell of the numerical model, could also be used as a prediction of the strength of the pitch angle scattering due to the whistler mode waves as a function of latitude. The pitch angle scattering will therefore be strongest over the range $-15° < \lambda < 15°$. Models of the latitudinal variation of anisotropy and warm plasma number density will have to become more sophisticated than those given in equations (1) and (2), but the best way to constrain these unknowns in the model would be to perform an observational survey, perhaps using Cluster or Polar data.

[25] Figure 8 shows that the origins of the largest amplitude waves are latitudinally separate from the location at which they are observed. Previous ray-tracing models assumed that whistler mode waves were generated directly (and only) at the equator [e.g., *Parrot et al.*, 2003, 2004; *Bortnik et al.*, 2007b; *Hayosh et al.*, 2010]. This may be true for whistler mode chorus, which most likely has a nonlinear generation mechanism that favors equatorial generation [e.g., *Omura and Nunn*, 2011]. However, it is unclear whether low-amplitude whistler mode waves are governed by the same physics. Our model predicts that given reasonable latitudinal variations of the warm plasma parameters, low-amplitude whistler mode waves could be generated over a range of latitudes.

[26] We propose that the low-amplitude whistler mode waves studied in this paper may be responsible for limiting particle flux in the magnetosphere [*Kennel and Petschek*, 1966; *Summers et al.*, 2009], or providing steady state electron precipitation at auroral latitudes [*Coroniti and Kennel*, 1970]. These phenomena rely on pitch angle

scattering of electrons and can occur over large volumes of the magnetosphere. The diffusion coefficient that describes the pitch angle scattering depends upon the details of the wave distribution [e.g., *Thorne et al.*, 2010]. We show that the largest path-integrated gains form a wave distribution that is different from that predicted by local solutions to the linear dispersion relation (see Figure 9b). Models of pitch angle diffusion may have to include such asymmetric wave distributions. However, the fact that these waves most likely result from conditions near marginal stability means that they will have very small amplitudes and be difficult to observe. Validating the model predictions may therefore prove challenging. The best strategy may be to seek periods of low magnetospheric activity where wave amplitudes are small [see, e.g., *Li et al.*, 2010, Figure 1] and this has been the motivation behind the current study. Models such as the one described in this paper may offer the best opportunity to study the delicate balance between the source of the observed equatorial temperature anisotropy, the marginal stability of whistler mode waves, the pitch angle scattering and the resulting diffuse electron precipitation, and provide a mechanism to study whistler mode wave growth and propagation over larger volumes than can be included in more sophisticated self-consistent numerical codes.

6. Conclusion

[27] We present ray-tracing analysis of the propagation and growth of whistler mode waves in the prenoon magnetosphere during low magnetospheric activity. We investigate millions of possible growing raypaths through a large volume using a plasma model constrained by a survey of THEMIS plasma parameters. Waves are only shown to pass through regions of the magnetosphere with $L > 8$ and are confined to a region with $-30° < \lambda < 30°$. Very few raypaths undergo magnetospheric reflection. Path-integrated gains peak at $L \sim 10$. The wave spectrum at large L in the magnetosphere is shown to be a superposition of waves from multiple initial locations with different histories. Typically, the largest path-integrated gain in any cell of the numerical model originates at a different latitude. The frequency range of the wave distribution at large L can be adequately described by the solutions of the local dispersion relation, but the range of wave normal angle is different. The wave distribution is also predicted to be asymmetric with respect to the wave normal angle. These results are important for the balance of stably trapped particle flux in the outer magnetosphere, and the control of diffuse electron precipitation at auroral latitudes.

Appendix A: The Number Density Model

[28] After *Inan and Bell* [1977], we use an isothermal diffusive equilibrium model, with an added plasmapause and lower ionospheric component given by

$$N_e(r, L) = N_{base} N_{DE} N_{LI} N_{PP}, \tag{A1}$$

where coordinates r and L give the radial distance from the centre of the Earth and the L number of the field line respectively. In the above model, $N_{base} = 9.1 \times 10^9$ m^{-3} is the electron number density at the base of the diffusive equilibrium model, and $N_{DE}(r)$ is the functional form of the diffusive equilibrium [*Angerami and Thomas*, 1964]

$$N_{DE}(r) = \left[\sum_{i=1}^{4} \delta_i e^{-z/H_i}\right]^{1/2}. \tag{A2}$$

Here, i indicates the number of species used in the model (hydrogen, helium and oxygen singly charged ions, as well as electrons), δ_i are the relative concentrations of each species at the base of the diffusive equilibrium model at r_b = 7371 km geocentric distance. We select 90% oxygen, 8% hydrogen and 2% helium. $z = r_b(1 - r_b/r)$, and H_i are the scale heights of each species, calculated assuming an ionospheric temperature of T = 0.138 eV.

[29] The lower ionosphere is incorporated using the following factor

$$N_{LI}(r) = 1 - \exp\left[-\left(\frac{(r - r_{LI})}{H_{LI}}\right)^2\right], \tag{A3}$$

where $r_{LI} = R_E + 90$ km is the geocentric distance to the level at the bottom of the lower ionosphere where the electron number density goes to zero and H_{LI} = 140 km is the scale height of the lower ionosphere. Finally, a plasmapause at L_p = 4.0 is added by assigning $N_{PP} = 1$ for $L < L_p$ and

$$N_{PP} = E_{PP} + (1 - E_{PP})R^a + (1 - R^a)E_c \tag{A4}$$

for $L \geq L_p$, where $R = r/r_c$, r_c = 5500 km, $a = -2.7$ is an exponent indicating the rate of decrease of number density outside the plasmapause and H_S = 500 km is the scale height of that decrease. The exponential terms in equation (A4) are

$$E_{PP} = \exp\left[-\left(\frac{L - L_p}{W}\right)\right], \tag{A5}$$

where W = 0.13 is the half-width of the plasmapause boundary, and

$$E_c = \exp\left[-\left(\frac{r - r_c}{H_S}\right)^2\right]. \tag{A6}$$

Note that L, L_p and W are all in units of Earth radius R_E.

[30] **Acknowledgments.** C.E.J.W. and A.W.D. are supported by the Canadian Space Agency.

[31] Robert Lysak thanks the reviewers for their assistance in evaluating this paper.

References

Abel, B., and R. M. Thorne (1998), Electron scattering loss in Earth's inner magnetosphere 1. Dominant physical processes, *J. Geophys. Res.*, *103*, 2385–2396.

Agapitov, O., V. Krasnoselskikh, Y. Zaliznyak, V. Angelopoulos, O. L. Contel, and G. Rolland (2010), Chorus source region localization in the Earth's outer magnetosphere using THEMIS measurements, *Ann. Geophys.*, *28*(6), 1377–1386.

Albert, J. M. (1999), Analysis of quasi-linear diffusion coefficients, *J. Geophys. Res.*, *104*, 2429–2441.

Albert, J. M. (2005), Evaluation of quasi-linear diffusion coefficients for whistler mode waves in a plasma with arbitrary density ratio, *J. Geophys. Res.*, *110*, A03218, doi:10.1029/2004JA010844.

Anger, C. D., R. R. Brown, D. S. Evans, and J. R. Barcus (1963), Long-period pulsations in electron precipitation associated with hydromagnetic waves in auroral zone, *J. Geophys. Res.*, *68*, 3306–3310.

Angerami, J. J., J. O. Thomas (1964), Studies of planetary atmospheres: 1. The distribution of electrons and ions in the Earth's exosphere, *J. Geophys. Res.*, *69*, 4537–4560.

Bekefi, G. (1966), *Radiation Processes in Plasmas*, 377 pp., John Wiley, New York.

Berkey, F. T. (1974), Coruscation of auroral particle flux at College, Alaska, *J. Atmos. Terr. Phys.*, *36*, 881–887.

Bhattacharya, B., R. M. Thorne, D. J. Williams, K. K. Khurana, and D. A. Gurnett (2005), Diffuse auroral precipitation in the Jovian upper atmosphere and magnetospheric electron flux variability, *Icarus*, *178*(2), 406–416.

Bortnik, J., U. S. Inan, and T. F. Bell (2006), Landau damping and resultant unidirectional propagation of chorus waves, *Geophys. Res. Lett.*, *33*, L03102, doi:10.1029/2005GL024553.

Bortnik, J., R. M. Thorne, and N. P. Meredith (2007a), Modeling the propagation characteristics of chorus using CRRES suprathermal electron fluxes, *J. Geophys. Res.*, *112*, A08204, doi:10.1029/2006JA012237.

Bortnik, J., R. M. Thorne, N. P. Meredith, and O. Santolík (2007b), Ray tracing of penetrating chorus and its implications for the radiation belts, *Geophys. Res. Lett.*, *34*, L15109, doi:10.1029/2007GL030040.

Bortnik, J., R. M. Thorne, and N. P. Meredith (2008), The unexpected origin of plasmaspheric hiss from discrete chorus emissions, *Nature*, *452*(7183), 62–66.

Bortnik, J., L. Chen, W. Li, R. M. Thorne, N. P. Meredith, and R. B. Horne (2011a), Modeling the wave power distribution and characteristics of plasmaspheric hiss, *J. Geophys. Res.*, *116*, A12209, doi:10.1029/2011JA016862.

Bortnik, J., L. Chen, W. Li, R. M. Thorne, and R. B. Horne (2011b), Modeling the evolution of chorus waves into plasmaspheric hiss, *J. Geophys. Res.*, *116*, A08221, doi:10.1029/2011JA016499.

Breneman, A. W., C. A. Kletzing, J. Pickett, J. Chum, and O. Santolík (2009), Statistics of multispacecraft observations of chorus dispersion and source location, *J. Geophys. Res.*, *114*, A06202, doi:10.1029/2008JA013549.

Brown, R. R. (1964), Study of slowly varying and pulsating ionospheric absorption events in auroral zone, *J. Geophys. Res.*, *69*, 2315–2321.

Brown, R. R. (1975), Further studies of long-period pulsations in ionospheric absorption at auroral zone latitudes, *J. Geophys. Res.*, *80*, 1023–1025.

Chen, L., R. M. Thorne, and R. B. Horne (2009), Simulation of EMIC wave excitation in a model magnetosphere including structured high-density plumes, *J. Geophys. Res.*, *114*, A07221, doi:10.1029/2009JA014204.

Chen, M., and M. Schulz (2001), Simulations of diffuse aurora with plasma sheet electrons in pitch angle diffusion less than everywhere strong, *J. Geophys. Res.*, *106*, 28,949–28,966.

Chum, J., and O. Santolík (2005), Propagation of whistler-mode chorus to low altitudes: Divergent ray trajectories and ground accessibility, *Ann. Geophys.*, *23*(12), 3727–3738.

Chum, J., F. Jiricek, J. Smilauer, and D. Shkyar (2003), Magion 5 observations of chorus-like emissions and their propagation features as inferred from ray-tracing simulation, *Ann. Geophys.*, *21*(12), 2293–2302.

Church, S. R., and R. M. Thorne (1983), On the origin of plasmaspheric hiss: Ray path integrated amplification, *J. Geophys. Res.*, *88*, 7941–7957.

Coroniti, F. V., and C. F. Kennel (1970), Electron precipitation pulsations, *J. Geophys. Res.*, *75*, 1279–1289.

Faith, J., S. Kuo, and J. Huang (1997a), Electron precipitation caused by chaotic motion in the magnetosphere due to large-amplitude whistler waves, *J. Geophys. Res.*, *102*, 2233–2241.

Faith, J., S. Kuo, J. Huang, and G. Schmidt (1997b), Precipitation of magnetospheric electrons caused by relativistic effect-enhanced chaotic motion in the whistler wave fields, *J. Geophys. Res.*, *102*, 9631–9638.

Gary, S. P., and J. Wang (1996), Whistler instability: Electron anisotropy upper bound, *J. Geophys. Res.*, *101*, 10,749–10,754.

Glauert, S. A., and R. B. Horne (2005), Calculation of pitch angle and energy diffusion coefficients with the PADIE code, *J. Geophys. Res.*, *110*, A04206, doi:10.1029/2004JA010851.

Hargreaves, J. K. (1969), Auroral absorption of HF radio waves in ionosphere: A review of results from first decade of riometry, *Proc. IEEE*, *57*(8), 1348–1373.

Hayakawa, M., M. Parrot, and F. Lefeuvre (1986), The wave normals of ELF hiss emissions observed onboard GEOS-1 at the equatorial and off-equatorial regions of the plasmasphere, *J. Geophys. Res.*, *91*, 7989–7999.

Hayosh, M., O. Santolík, and M. Parrot (2010), Location and size of the global source region of whistler mode chorus, *J. Geophys. Res.*, *115*, A00F06, doi:10.1029/2009JA014950.

Heacock, R. R., and R. D. Hunsucker (1977), Study of concurrent magnetic-field and particle precipitation pulsations, 0.005 to 0.5 Hz, recorded near College, Alaska, *J. Atmos. Terr. Phys.*, *39*(4), 487–501.

Hikishima, M., S. Yagitani, Y. Omura, and I. Nagano (2009a), Full particle simulation of whistler-mode rising chorus emissions in the magnetosphere, *J. Geophys. Res.*, *114*, A01203, doi:10.1029/2008JA013625.

Hikishima, M., S. Yagitani, Y. Omura, and I. Nagano (2009b), Coherent nonlinear scattering of energetic electrons in the process of whistler mode chorus generation, *J. Geophys. Res.*, *114*, A10205, doi:10.1029/2009JA014371.

Horne, R. B., and R. M. Thorne (1997), Wave heating of He^+ by electromagnetic ion cyclotron waves in the magnetosphere: Heating near the H^+-He^+ bi-ion resonance frequency, *J. Geophys. Res.*, *102*, 11,457–11,471.

Horne, R. B., and R. M. Thorne (1998), Potential waves for relativistic electron scattering and stochastic acceleration during magnetic storms, *Geophys. Res. Lett.*, *25*, 3011–3014.

Horne, R. B., and R. M. Thorne (2000), Electron pitch angle diffusion by electrostatic electron cyclotron harmonic waves: The origin of pancake distributions, *J. Geophys. Res.*, *105*, 5391–5402.

Horne, R. B., and R. M. Thorne (2003), Relativistic electron acceleration and precipitation during resonant interactions with whistler-mode chorus, *Geophys. Res. Lett.*, *30*(10), 1527, doi:10.1029/2003GL016973.

Horne, R. B., R. M. Thorne, N. P. Meredith, and R. R. Anderson (2003), Diffuse auroral electron scattering by electron cyclotron harmonic and whistler mode waves during an isolated substorm, *J. Geophys. Res.*, *108*(A7), 1290, doi:10.1029/2002JA009736.

Hospodarsky, G. B., T. F. Averkamp, W. S. Kurth, D. A. Gurnett, M. Dougherty, U. Inan, and T. Wood (2001), Wave normal and Poynting vector calculations using the Cassini radio and plasma wave instrument, *J. Geophys. Res.*, *106*, 30,253–30,269.

Huang, C. Y., and C. K. Goertz (1983), Ray-tracing studies and path-integrated gains of ELF unducted whistler mode waves in the Earth's magnetosphere, *J. Geophys. Res.*, *88*, 6181–6187.

Huang, C. Y., C. K. Goertz, and R. R. Anderson (1983), A theoretical-study of plasmaspheric hiss generation, *J. Geophys. Res.*, *88*, 7927–7940.

Hunsucker, R. D., H. F. Bates, and A. E. Belon (1972), Observations of simultaneous auroral D and E layers with incoherent scatter radar, *Nature*, *239*(94), 102–104.

Inan, U. S. (1987), Gyroresonant pitch angle scattering by coherent and incoherent whistler mode waves in the magnetosphere, *J. Geophys. Res.*, *92*, 127–142.

Inan, U. S., and T. F. Bell (1977), Plasmapause as a VLF wave guide, *J. Geophys. Res.*, *82*, 2819–2827.

Inan, U. S., Y. T. Chiu, and G. T. Davidson (1992), Whistler-mode chorus and morningside aurorae, *Geophys. Res. Lett.*, *19*, 653–656.

Jordanova, V. K., J. Albert, and Y. Miyoshi (2008), Relativistic electron precipitation by EMIC waves from self-consistent global simulations, *J. Geophys. Res.*, *113*, A00A10, doi:10.1029/2008JA013239.

Katoh, Y., and Y. Omura (2007), Computer simulation of chorus wave generation in the Earth's inner magnetosphere, *Geophys. Res. Lett.*, *34*, L03102, doi:10.1029/2006GL028594.

Katoh, Y., and Y. Omura (2011), Amplitude dependence of frequency sweep rates of whistler-mode chorus emissions, *J. Geophys. Res.*, *116*, A07201, doi:10.1029/2011JA016496.

Kennel, C. F., and H. E. Petschek (1966), Limit on stably trapped particle fluxes, *J. Geophys. Res.*, *71*(1), 1–28.

Kimura, I. (1966), Effects of ions on whistler-mode ray tracing, *Radio Sci.*, *1*, 269–283.

Kimura, I. (1985), Whistler mode propagation in the Earth and planetary magnetospheres and ray tracing techniques, *Space Sci. Rev.*, *42*, 449–466.

Kirkwood, S., and A. Osepian (2001), Pitch angle diffusion coefficients and precipitating electron fluxes inferred from EISCAT radar measurements at auroral latitudes, *J. Geophys. Res.*, *106*, 5565–5578.

Kuo, S. P., S. S. Kuo, J. T. Huynh, and P. Kossey (2007), Precipitation of trapped relativistic electrons by amplified whistler waves in the magnetosphere, *Phys. Plasmas*, *14*, 062903.

Lam, M. M., R. B. Horne, N. P. Meredith, S. A. Glauert, T. Moffat-Griffin, and J. C. Green (2010), Origin of energetic electron precipitation >30 keV into the atmosphere, *J. Geophys. Res.*, *115*, A00F08, doi:10.1029/2009JA014619.

LeContel, O., et al. (2009), Quasi-parallel whistler mode waves observed by THEMIS during near-Earth dipolarizations, *Ann. Geophys.*, *27*(6), 2259–2275.

LeDocq, M. J., D. A. Gurnett, and G. B. Hospodarsky (1998), Chorus source locations from VLF Poynting flux measurements with the Polar spacecraft, *Geophys. Res. Lett.*, *25*(21), 4063–4066.

Li, W., R. M. Thorne, N. P. Meredith, R. B. Horne, J. Bortnik, Y. Y. Shprits, and B. Ni (2008), Evaluation of whistler mode chorus amplification during an injection event observed on CRRES, *J. Geophys. Res.*, *113*, A09210, doi:10.1029/2008JA013129.

Li, W., et al. (2009), Evaluation of whistler-mode chorus intensification on the nightside during an injection event observed on the THEMIS spacecraft, *J. Geophys. Res.*, *114*, A00C14, doi:10.1029/2008JA013554.

Li, W., et al. (2010), THEMIS analysis of observed equatorial electron distributions responsible for the chorus excitation, *J. Geophys. Res.*, *115*, A00F11, doi:10.1029/2009JA014845.

Liemohn, M. W., G. V. Khazanov, and J. U. Kozyra (1997), Guided plasmaspheric hiss interactions with superthermal electrons 1. Resonance curves and timescales, *J. Geophys. Res.*, *102*, 11,619–11,623.

Lorentzen, K. R., J. B. Blake, U. S. Inan, and J. Bortnik (2001), Observations of relativistic electron microbursts in association with VLF chorus, *J. Geophys. Res.*, *106*, 6017–6027.

Lyons, L. R. (1974a), Pitch angle and energy diffusion-coefficients from resonant interactions with ion-cyclotron and whistler waves, *J. Plasma Phys.*, *12*, 417–432.

Lyons, L. R. (1974b), General relations for resonant particle diffusion in pitch angle and energy, *J. Plasma Phys.*, *12*, 45–49.

Meredith, N. P., R. B. Horne, R. M. Thorne, and R. R. Anderson (2009), Survey of upper band chorus and ECH waves: Implications for the diffuse aurora, *J. Geophys. Res.*, *114*, A07218, doi:10.1029/2009JA014230.

Miyoshi, Y., K. Sakaguchi, K. Shiokawa, D. Evans, J. Albert, M. Connors, and V. Jordanova (2008), Precipitation of radiation belt electrons by EMIC waves, observed from ground and space, *Geophys. Res. Lett.*, *35*, L23101, doi:10.1029/2008GL035727.

Miyoshi, Y., Y. Katoh, T. Nishiyama, T. Sakanoi, K. Asamura, and M. Hirahara (2010), Time of flight analysis of pulsating aurora electrons, considering wave-particle interactions with propagating whistler mode waves, *J. Geophys. Res.*, *115*, A10312, doi:10.1029/2009JA015127.

Muto, H., and M. Hayakawa (1987), Ray-tracing study of the propagation in the magnetosphere of whistler-mode VLF emissions with frequency above one half the gyrofrequency, *Planet. Space Sci.*, *35*(11), 1397–1404.

Muto, H., M. Hayakawa, M. Parrot, and F. Lefeuvre (1987), Direction finding of half-gyrofrequency VLF emissions in the off-equatorial region of the magnetosphere and their generation and propagation, *J. Geophys. Res.*, *92*, 7538–7550.

Nagano, I., S. Yagitani, H. Kojima, and H. Matsumoto (1996), Analysis of wave normal and Poynting vectors of the chorus emissions observed by Geotail, *J. Geomagn. Geoelectr.*, *48*(3), 299–307.

Ni, B., R. M. Thorne, Y. Y. Shprits, and J. Bortnik (2008), Resonant scattering of plasma sheet electrons by whistler-mode chorus: Contribution to diffuse auroral precipitation, *Geophys. Res. Lett.*, *35*, L11106, doi:10.1029/2008GL034032.

Nunn, D., O. Santolík, M. Rycroft, and V. Trakhtengerts (2009), On the numerical modeling of VLF chorus dynamical spectra, *Ann. Geophys.*, *27*, 2341–2359.

Olson, J. V., G. Rostoker, and G. Olchowy (1980), A study of concurrent riometer and magnetometer variations in the Pc 4-5 pulsation band, *J. Geophys. Res.*, *85*, 1695–1702.

Omura, Y., and D. Nunn (2011), Triggering process of whistler mode chorus emissions in the magnetosphere, *J. Geophys. Res.*, *116*, A05205, doi:10.1029/2010JA016280.

Omura, Y., Y. Katoh, and D. Summers (2008), Theory and simulation of the generation of whistler-mode chorus, *J. Geophys. Res.*, *113*, A04223, doi:10.1029/2007JA012622.

Omura, Y., M. Hikishima, Y. Katoh, D. Summers, and S. Yagitani (2009), Nonlinear mechanisms of lower-band and upper-band VLF chorus emissions in the magnetosphere, *J. Geophys. Res.*, *114*, A07217, doi:10.1029/2009JA014206.

Paquette, J. A., D. L. Matthews, T. J. Rosenberg, L. J. Lanzerotti, and U. S. Inan (1994), Source regions of long-period pulsation events in electron precipitation and magnetic fields at South Pole Station, *J. Geophys. Res.*, *99*, 3869–3877.

Parrot, M., O. Santolík, N. Cornilleau-Wehrlin, M. Maksimovic, and C. C. Harvey (2003), Source location of chorus emissions observed by Cluster, *Ann. Geophys.*, *21*, 473–480.

Parrot, M., O. Santolík, D. A. Gurnett, J. S. Pickett, and N. Cornilleau-Wehrlin (2004), Characteristics of magnetospherically reflected chorus waves observed by Cluster, *Ann. Geophys.*, *22*, 2597–2606.

Parthasarathy, R., and V. P. Hessler (1964), Periodic covariation of radio wave absorption Earth currents and other associated phenomena in auroral zone, *J. Geophys. Res.*, *69*, 2867–2871.

Posch, J. L., M. J. Engebretson, A. T. Weatherwax, D. L. Detrick, W. J. Hughes, and C. G. Maclennan (1999), Characteristics of broadband ULF magnetic pulsations at conjugate cusp latitude stations, *J. Geophys. Res.*, *104*, 311–331.

Press, W. H., S. A. Teukolsky, W. T. Vetterling, and B. P. Flannery (2007), *Numerical Recipes: The Art of Scientific Computing*, Cambridge Univ. Press, Cambridge, U. K.

Radioti, A., A. T. Tomas, D. Grodent, J. C. Gerard, J. Gustin, B. Bonford, N. Krupp, J. Woch, and J. D. Menietti (2009), Equatorward diffuse auroral emissions at Jupiter: Simultaneous HST and Galileo observations, *Geophys. Res. Lett.*, *36*, L07101, doi:10.1029/2009GL037857.

Rae, I. J., I. R. Mann, Z. C. Dent, D. K. Milling, E. F. Donovan, and E. Spanswick (2007), Multiple field line resonances: Optical, magnetic and absorption signatures, *Planet. Space Sci.*, *55*, 701–713.

Roldugin, V. C., and A. V. Roldugin (2008), Pc5 pulsations on the ground, in the magnetosphere, and in the electron precipitation: Event of 19 January 2005, *J. Geophys. Res.*, *113*, A04222, doi:10.1029/2007JA012553.

Santolík, O., M. Parrot, L. R. O. Storey, J. S. Pickett, and D. A. Gurnett (2001), Propagation analysis of plasmaspheric hiss using Polar PWI measurements, *Geophys. Res. Lett.*, *28*, 1127–1130, doi:10.1029/2000GL012239.

Santolík, O., D. A. Gurnett, J. S. Pickett, M. Parrot, and N. Cornilleau-Wehrlin (2003), Spatio-temporal structure of storm-time chorus, *J. Geophys. Res.*, *108*(A7), 1278, doi:10.1029/2002JA009791.

Santolík, O., D. A. Gurnett, J. S. Pickett, J. Chum, and N. Cornilleau-Wehrlin (2009), Oblique propagation of whistler mode waves in the chorus source region, *J. Geophys. Res.*, *114*, A00F03, doi:10.1029/2009JA014586.

Schulz, M., and L. J. Lanzerotti (1974), *Particle Diffusion in the Radiation Belts*, 215 pp., Springer, New York.

Shprits, Y. Y., W. Li, and R. M. Thorne (2006), Controlling effect of the pitch angle scattering rates near the edge of the loss cone on electron lifetimes, *J. Geophys. Res.*, *111*, A12206, doi:10.1029/2006JA011758.

Spanswick, E., E. Donovan, and G. Baker (2005), Pc5 modulation of high energy electron precipitation: Particle interaction regions and scattering efficiency, *Ann. Geophys.*, *23*, 1533–1542.

Stix, T. H. (1992), *Waves in Plasmas*, 566 pp., Am. Inst. of Phys., New York.

Su, Z., H. Zheng, and S. Wang (2010), A parametric study on the diffuse auroral precipitation by resonant interaction with whistler mode chorus, *J. Geophys. Res.*, *115*, A05219, doi:10.1029/2009JA014759.

Summers, D., and R. M. Thorne (2003), Relativistic electron pitch angle scattering by electromagnetic ion cyclotron waves during geomagnetic storms, *J. Geophys. Res.*, *108*(A4), 1143, doi:10.1029/2002JA009489.

Summers, D., C. Ma, and T. Mukai (2004), Competition between acceleration and loss mechanisms of relativistic electrons during geomagnetic storms, *J. Geophys. Res.*, *109*, A04221, doi:10.1029/2004JA010437.

Summers, D., B. Ni, and N. P. Meredith (2007a), Timescales for radiation belt electron acceleration and loss due to resonant wave-particle interactions: 1. Theory, *J. Geophys. Res.*, *112*, A04206, doi:10.1029/2006JA011801.

Summers, D., B. Ni, and N. P. Meredith (2007b), Timescales for radiation belt electron acceleration and loss due to resonant wave-particle interactions: 2. Evaluation for VLF chorus, ELF hiss, and electromagnetic ion cyclotron waves, *J. Geophys. Res.*, *112*, A04207, doi:10.1029/2006JA011993.

Summers, D., B. Ni, N. P. Meredith, R. B. Horne, R. M. Thorne, M. B. Moldwin, and R. R. Anderson (2008), Electron scattering by whistler-mode ELF hiss in plasmaspheric plumes, *J. Geophys. Res.*, *113*, A04219, doi:10.1029/2007JA012678.

Summers, D., R. Tang, and R. M. Thorne (2009), Limit on stably trapped particle fluxes in planetary magnetospheres, *J. Geophys. Res.*, *114*, A10210, doi:10.1029/2009JA014428.

Tadokoro, H., F. Tsuchiya, Y. Miyoshi, Y. Katoh, A. Morioka, and H. Misawa (2009), Storm-time electron flux precipitation in the inner radiation belt caused by wave-particle interactions, *Ann. Geophys.*, *27*, 1669–1677.

Thorne, R. M., S. R. Church, and D. J. Gorney (1979), Origin of plasmaspheric hiss: The importance of wave-propagation and the plasmapause, *J. Geophys. Res.*, *84*, 5241–5247.

Thorne, R. M., T. P. O'Brien, Y. Y. Shprits, D. Summers, and R. B. Horne (2005), Timescale for MeV electron microburst loss during geomagnetic storms, *J. Geophys. Res.*, *110*, A09202, doi:10.1029/2004JA010882.

Thorne, R. M., B. Ni, X. Tao, R. B. Horne, and N. P. Meredith (2010), Scattering by chorus waves as the dominant cause of diffuse auroral precipitation, *Nature*, *467*(7318), 943–946.

Tkalcevic, S., U. S. Inan, and R. A. Helliwell (1984), Nonlinear pitch angle scattering and trapping of energetic particles during Landau resonance interactions with whistler mode waves, *J. Geophys. Res.*, *89*, 813–826.

Trakhtengerts, V. Y., and M. J. Rycroft (2008), *Whistler and Alfven Mode Cyclotron Masers in Space*, 354 pp., Cambridge Univ. Press, Cambridge, U. K.

Tripathi, A. K., and R. P. Singhal (2008), Whistler-mode instability in magnetospheres of Uranus and Neptune, *Planet. Space Sci.*, *56*(3–4), 310–319.

Tsurutani, B. T., and E. J. Smith (1977), Two types of magnetospheric ELF chorus and their substorm dependences, *J. Geophys. Res.*, *82*, 5112–5128.

Villalon, E., and W. J. Burke (1995), Pitch-angle scattering of diffuse auroral electrons by whistler-mode waves, *J. Geophys. Res.*, *100*, 19,361–19,369.

Walter, F. (1969), Nonducted VLF propagation in the magnetosphere, PhD thesis, Stanford Univ., Stanford, Calif.
Watt, C. E. J., A. W. Degeling, R. Rankin, K. R. Murphy, I. J. Rae, and H. J. Singer (2011), Ultralow-frequency modulation of whistler-mode wave growth, *J. Geophys. Res.*, *116*, A10209, doi:10.1029/2011JA016730.
Xiao, F., R. M. Thorne, D. A. Gurnett, and D. J. Williams (2003), Whistler-mode excitation and electron scattering during an interchange event near Io, *Geophys. Res. Lett.*, *30*(14), 1749, doi:10.1029/2003GL017123.
Xiao, F. L., and X. S. Feng (2006), Modeling density and anisotropy of energetic electrons along magnetic field lines, *Plasma Sci. Technol.*, *8*(3), 279–284.
Yuan, F. F. F., and F. Jacka (1969), Simultaneous geomagnetic and cosmic noise absorption pulsations near geomagnetic noon, *Nature*, *222*(5194), 653–654.
Ziauddin, S. (1960), Simultaneous observations of pulsations in the geomagnetic field and in ionospheric absorption, *Can. J. Phys.*, *38*(12), 1714–1715.